Effect of precursor composition and heat-treatment on the morphology and physical properties of Ag nanosponges

Sanaa A. Alzahrani [a,b], Kaludewa S.B. De Silva [a], Annette Dowd [a,*], Matthew D. Arnold [a], Michael B. Cortie [c]

[a] School of Mathematical and Physical Sciences, University of Technology Sydney, PO Box 123, Ultimo, NSW, 2007, Australia
[b] Department of Physics, Al-Lith University College, Umm Al-Qura University, Makkah, Saudi Arabia
[c] School of Mechanical, Materials, Mechatronic and Biomedical Engineering, University of Wollongong, Australia

ARTICLE INFO

ABSTRACT

Nanoporous silver (np-S) was prepared by free corrosion dealloying of a series of Ag–Al thin films containing between 25 and 73 at.% Al. It was found that precursor composition had an important influence on the nano-structures and morphologies of the np-S. In particular the size of the Ag ligaments systematically decreased from 32 to 13 nm as the Al content was increased over the series. In contrast, there was only a weak effect on pore size, which remained in the range 11–15 nm, with the maximum occurring at about 55 at.% Al. There was however a significant increase in the density of the pores as the Al content of the precursor was increased. The electrical resistivity of the np-S increases with the decrease in ligament size, changing from about 3×10^{-8} Ω m for sponges with ligaments of about 32 nm diameter rising to 30×10^{-8} Ω m for the sponge with the 13 nm ligaments. The surface area of the np-S was estimated by the electrochemical capacitance in KNO_3 solutions and was estimated to increase by an order of magnitude compared to a smooth Ag surface. There was a systematic change in the optical properties of the sponges, with a trend towards less metallic behaviour as the ligament size decreased and pore density increased. These changes culminated in the sponge prepared from the 73 at.% Al precursor having non-metallic characteristics with regard to visible and near-infrared light. The volume fraction of metal was estimated to be of the order of 40 ± 5%. Prior annealing of the precursor inhibited dealloying.

1. Introduction

In general, nano-porous sponges of metallic elements are unstable in air and oxidize rapidly. The exceptions are the nano-porous sponges of the precious metals. The most important characteristic of a nano-porous material is its very high ratio of surface area to volume or mass. Additional phenomena such as enhanced surface chemical reactivity, altered electrical conductivity or unusual optical properties may also be present. As a result, these materials have become of interest in fields as diverse as chemical catalysis, supercapacitors, electrodes for fuel cells or lithium ion batteries, sensors, actuation, spectrally-selective coatings or as substrates on which to conduct surface-enhanced Raman spectroscopy (SERS) (Cortie et al., 2007; Mortari et al., 2007; Yuan et al., 2007; Wittstock et al., 2012; Zhang and Li, 2012; Ron et al., 2018; Ding and Zhang, 2016).

The morphology of nano-porous sponges (strictly speaking, these are *mesoporous* sponges if one follows the nomenclature guidelines of IUPAC

(Haber, 1991; Sing, 1985)) is very variable. The most frequently encountered type is the fibrous sponge (consisting of a bi-continuous vermicular architecture of ligaments and channels), but foamy sponges (continuous metal matrix containing percolating spherical voids), anisotropic cracked sponges (in which the cavities are aligned), anisotropic pinhole sponges (in which the pores and tunnels are not percolated), and anisotropic columnar sponges (in which both solid and cavity possess a mutual preferred orientation) have also been reported (Supansomboon et al., 2014).

Many strategies have been developed for producing metallic nano-porous sponges, such as thermal decomposition (Li et al., 2016a; Zhao et al., 2008), templating (Luechinger et al., 2010; Wu et al., 2022; Zheng et al., 2013), deposition into a metal-organic framework (Walsh et al., 2003; Abednatanzi et al., 2015; Jiang et al., 2015; Li et al., 2019; Salunkhe et al., 2017), or dealloying of a precursor alloy (Forty, 1979; Erlebacher et al., 2001). Due to its high productivity and controllability, the dealloying method has arguably become the most efficient way to
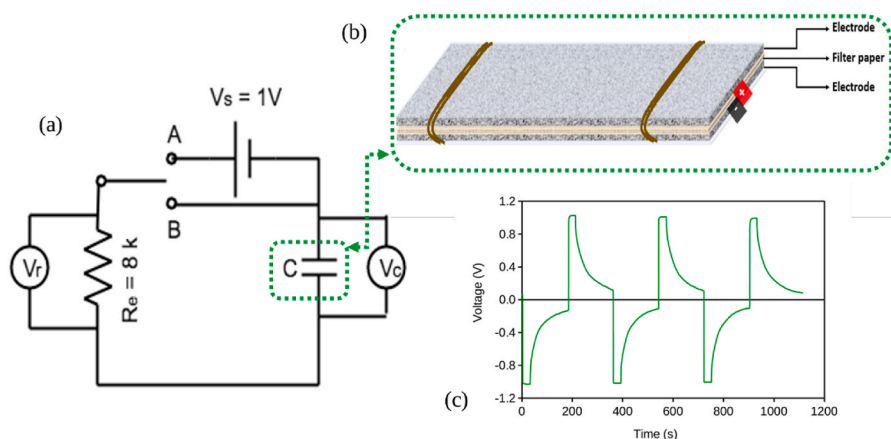
Fig. 1. (a) The R–C circuit used to charge and discharge the capacitor. When the switch is connected at position A, the power supply voltage V_s is equal to sum of the voltage at the terminals of the capacitor V_c and the voltage of the external resistance V_r at this point. Discharge through the resistor is achieved by changing the switch to position B. (b) Schematic diagram of the supercapacitors which were made with a sandwich of np-S thin film electrodes with a piece of filter paper as spacer. (c) the polarity of alternate cycles was reversed in order to permit symmetrical changes (if any) to occur on the electrodes.
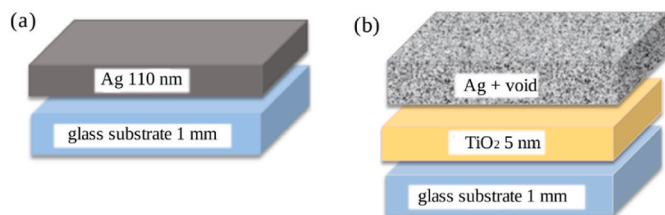
Fig. 2. schematic drawing of (a) the three-layer model for analysing SE spectra of de-alloyed thin films.

Table 1

Composition and constituents of precursor and dealloyed thin films. For comparison, the calculated equilibrium amount of Ag_2Al at 500 °C is also shown.

	S1	S2	S3	S4	S5	S6
As deposited						
Al, at.%	24.6	33.8	42.2	52.6	62.3	72.6
Approx. wt.% Ag_2Al, XRD	0	25–30	45–55	38–46	0	0
Equilibrium Ag_2Al, wt.%	100	100	75	65	53	36
As-deposited then dealloyed						
Al, at%	1.8	5.6	5.4	3.9	3.7	1.4
Approx. wt.% Ag_2Al, XRD	0	0	0–30	0	0–30	0
Equilibrium Ag_2Al, wt.%	0	0	0	0	0	0
Annealed						
Al, at.%	29.4	39.1	59.7	65.5	78.5	85.2
Approx. wt.% Ag_2Al, XRD	0	35–65	52–70	60–70	75–90	82–92
Equilibrium Ag_2Al, wt.%	85	78	57	48	24	5
Annealed then dealloyed						
Al, at%	6.1	10.1	25.7	43.1	54.6	71.7
Approx. wt.% Ag_2Al, XRD	0	70–80	80–90	65–75	90–99	90–99
Equilibrium Ag_2Al, wt.%	0	0	100	75	63	38

fabricate nano-porous metals including nano-porous silver (np-S) (Liu et al., 2018). The process of dealloying involves the selective dissolution of electrochemically active surface atoms and diffusion and aggregation of the remaining noble surface atoms (Detsi et al., 2013; Hakamada and Mabuchi, 2009; Kurowska-Tabor et al., 2016; Qiu et al., 2011; Zhang et al., 2019; Zhao et al., 2008; Zou et al., 2018). Although an anodic

potential can be applied to accelerate the dealloying, it is also very common to allow it to proceed under free corrosion conditions. In general, formation of a nano-porous metallic sponge by de-alloying requires use of a precursor alloy that consists of a more noble metal (for example Au, Pt, or Ag) and a sacrificial metal (for example Al, Mg or Zn). The inner architecture and overall properties of the nano-porous metals can, in principle, be tailored by varying the concentration of the noble metal. In general, a large difference in the electrochemical potentials of the noble and sacrificial metals is needed (Zhang and Ying, 2017), and the alloys should usually contain 60 at.% or more of the reactive element or else they may take too long to dealloy, if they do so at all. It is usually accepted that, if a homogenous sponge is required, then the starting alloy should also be single phase (Ding and Zhang, 2016; Zhang et al., 2009).

Although alloy systems such as Ag–Zn (Li et al., 2013), Ag–Cu (Wang et al., 2019) and Ag–Al (Detsi et al., 2012; Liu et al., 2018; Qiu et al., 2011; Song et al., 2011; Wang et al., 2009), or ternary Ag–Mg–Ca (Li et al., 2016b) have been used to fabricate three-dimensional, bi-continuous and open porous structures of nanoporous silver (np-S), the selective chemical etching of Ag–Al is currently the most popular. This is due to the direct and rapid dissolution of Al in acidic or alkaline aqueous solution under free corrosion conditions (Cortie et al., 2007) due to the large difference in standard reduction potentials between Ag and Al components (respectively +0.80V and −1.71 V vs hydrogen). Concentrations of Al generally range from 50 to 95 at.%. As examples, Detsi et al. (2012) have succeeded in the production of np-S films with ligament sizes between 30 nm and 60 nm through chemical dealloying of Ag–Al alloys in HCl, Wang et al., 2009 have obtained np-S with ligament sizes between 95 nm and 450 nm by dealloying Ag–Al ingots in HCl or NaOH solution while Song et al. (2011) dealloyed melt-spun Ag–Al ribbons in H_2SO_4, H_3PO_4, $C_2H_2O_4$ or HCl to form np-S with ligament sizes between 138 and 331 nm. (More examples of prior work are listed in Table S1 of the Supplementary Material). The specific surface area of the sponges obtained varies between 3 and 11 m^2g^{-1}. The characteristic ligament sizes and specific surface areas of np-S have generally been rather large however when compared to the finer-scale features obtainable in nano-porous Au (Detsi et al., 2012). In general, even smaller pore and ligament sizes would be desirable to enhance the properties of np-S (Detsi et al., 2012).

Most prior work on np-S made from $Ag_{1-x}Al_x$ precursors has focussed on dealloying specific, fixed, compositions of precursor produced by casting or melt spinning (Wang et al., 2009; Zhang et al., 2009; Zhang and Zhang, 2010; Song et al., 2011; Qiu et al., 2011; Wu et al., 2015; Luo et al., 2020). Unfortunately, melt-route samples of Ag–Al alloys will
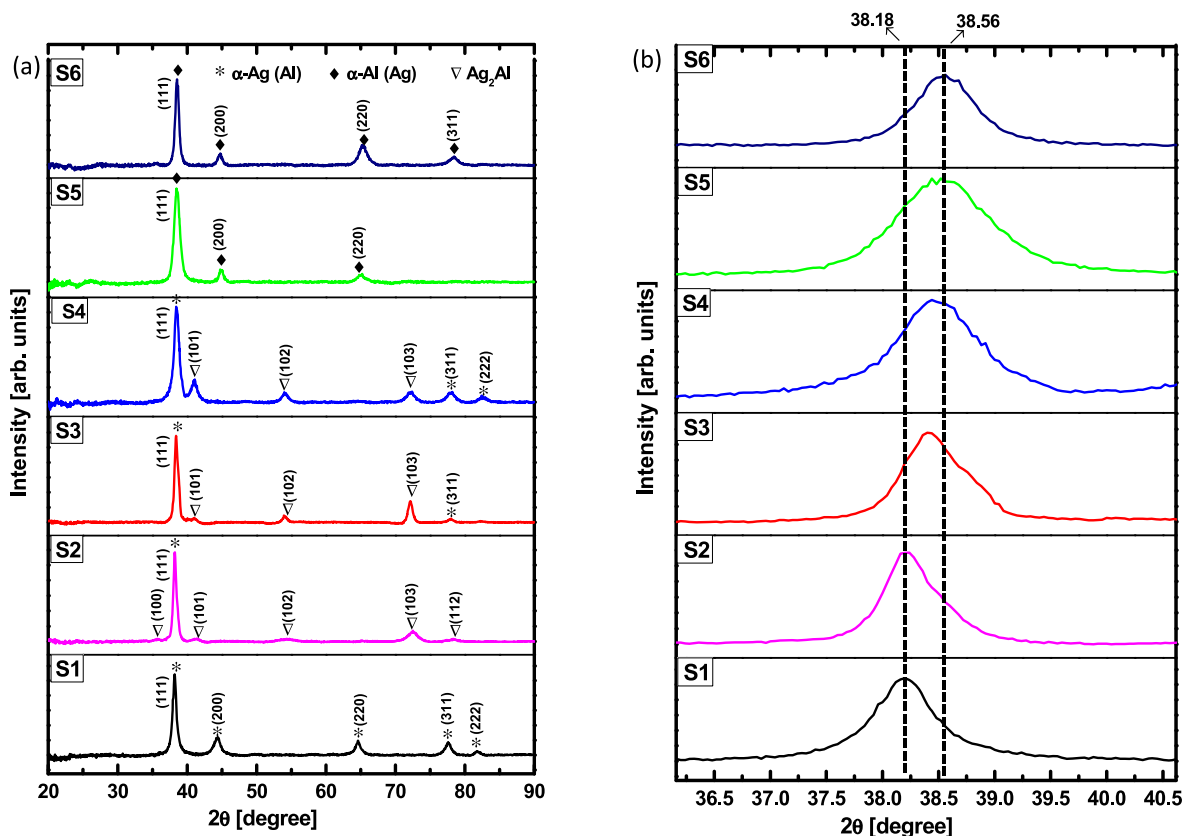
Fig. 3. XRD pattern of a) the as-deposited Al_xAg_{100-x} alloy thin films with different Al concentrations, the peaks are marked by different shapes of scatters representing different phases, b) enlarged (111) diffraction peak of the as-deposited alloy thin films showing a small shift of that stronger peak with increasing Al concentration.
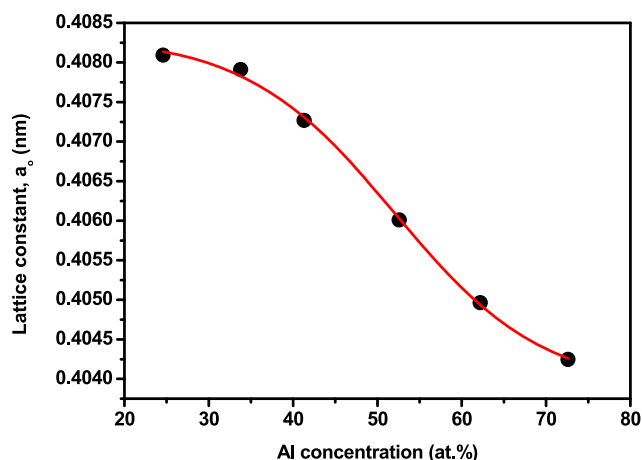
Fig. 4. variation in lattice constant of the as-deposited alloys as a function of changing the Al concentrations, it clearly shows that the lattice parameter values decrease with increasing Al concentration.

generally contain significant microstructural segregation of Al due to the very flat liquidus and solidus curves on the Al-rich side of the binary phase diagram. The segregation may not be completely suppressed even for melt-spun ribbons. In contrast, co-sputtering of the elements using magnetron sputtering at room temperature generates a metastable deposit that is almost homogeneous. This is due to the very low rates of diffusion in the solid material at the temperature of deposition. Here we have exploited this property of magnetron sputtered coatings to fabricate a series of $Ag_{1-x}Al_x$ alloy thin films with between 24.6 and 72.6 at.%

Al. After dealloying, the morphology and physical properties of the films were extensively investigated. Parameters of interest included the pore and ligament sizes, electrical conductivity, and optical properties. Optical properties were also investigated because they are a sensitive indicator of nanoscale structure. Spectroscopic ellipsometry was used to measure the relative dielectric permittivity of the films and the results compared to a numerical model based on the Bruggeman effective medium theory.

2. Material and methods

2.1. Sample preparation

The $Ag_{1-x}Al_x$ thin-film alloys were magnetron co-sputtered onto glass substrates at room temperature. Prior to deposition of the alloys, the substrates were cleaned using an antibacterial spray followed by 20 min each of ultrasonic cleaning in acetone, ethanol, and reverse osmosis (RO) water. Finally, the substrates were blown dry using N_2. The composition of the film was controlled by varying the deposition rate of Al while the rate of deposition of Ag was held constant. The deposition times were adjusted so that the precursor films would all be nominally 110 nm thick. The sputtering chamber was evacuated to a base pressure of 4.7×10^{-4} Pa. The working gas was argon. During the sputtering process, the substrates were rotated at 12 rev/min to promote uniform film growth. The distance between the targets and sample holder was fixed at 110 mm, with an angle of 60°. The glass substrate was sputtered with three layers, consisting nominally of 5 nm of Ti as an adhesion layer (first layer), 3 nm of Ag (second layer), and 100 nm of Ag–Al alloy (top layer). The actual thin films obtained were typically of the order of 115–120 nm in thickness. Further information regarding the deposition parameters is provided as Tables S2 and S3 in the Supplementary
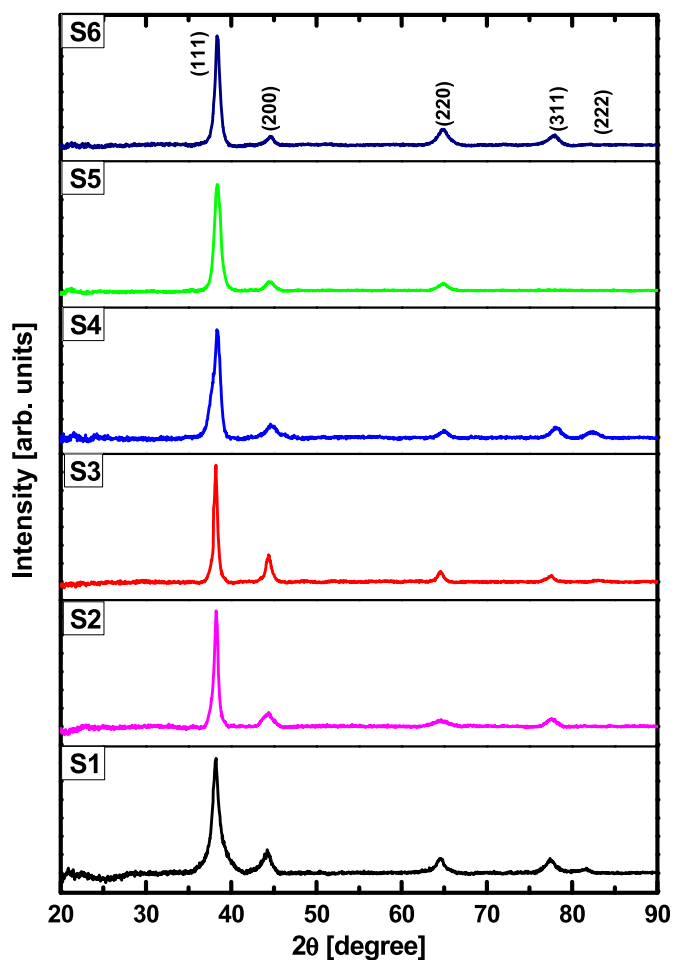
Fig. 5. XRD pattern of the de-alloyed Al_xAg_{100-x} thin film alloys in 1 M NaOH solution. The present peaks are assigned to diffraction from the (111), (200), (220), (311) and (222) planes of single phase which is silver.

Material.

Dealloying was carried out in 1 M NaOH aqueous solution at room temperature for 13, 9, 7, 6, 3 and 2 min respectively for samples S1, S2, S3, S4, S5 and S6. Dealloying in NaOH concentration higher than 1M led to the film peeling off, while dealloying at much lower NaOH concentrations resulting in a high concentration of residual Al even when dealloying was conducted for a long period of time. The as-dealloyed samples were rinsed with deionised (DI) water, dried by ethanol and then stored in a vacuum desiccator. Films were characterized in the as-deposited state and after dealloying. The effect of an anneal in a forming gas atmosphere at 500 °C for 60 min to enhance the crystallisation of the precursor films was also investigated.

2.2. Characterisation of sample microstructure

The nanostructure of the sponge was characterised using the following techniques: Energy Dispersive X-ray Spectroscopy (EDS) was carried out using an Evo LS15 scanning electron microscope equipped with a Bruker SDD XFlash 5030 detector (Carl Zeiss Microscopy Deutschland GmbH, Oberkochen, Germany). A 15 kV accelerating voltage and a working distance of 10 mm were applied. To express the elemental compositions of the thin-film alloys with sufficient reliability, the EDS measurements were replicated and carried out at five different locations on each thin-film alloy to find out the relative standard deviations (RSD) of the EDS measurements using Eq. (1) (Miler and Mirtič, 2013):

$$\mathrm{RSD}\ (\%) = \left(\frac{\sigma_{\mathrm{at}}}{x_{\mathrm{av}}}\right) \times 100\% \tag{1}$$

where σ_{at} is the standard deviation of replicated the EDS measurements and x_{av} is the mean content of the element.

The surface topography of the samples was imaged using a Supra 55VP scanning electron microscope equipped with a Schottky field emission gun and an in-lens detector for high-resolution images operating at 5 kV (Carl Zeiss Microscopy Deutschland GmbH, Oberkochen, Germany). A D8 Discover X-ray diffractometer equipped with copper K-alpha (Cu Kα, wavelength of 1.5418 Å), a primary beam monochromator, and a LYNXEYE_XE (0D mode) detector (Bruker, Billerica, Massachusetts, USA) were used to obtain XRD patterns for determining the crystallographic structure and the crystalline phases present in the alloys. The XRD patterns were collected with a grazing incidence angle of 1° and a 2θ-α angle ranging from 20° to 90°. Rietveld refinement was conducted using FULLPROF (https://www.ill.eu/sites/fullprof/) which was called through the MATCH! (Crystal Impact, Bonn, Germany) interface. While satisfactory for single phase materials, the refinement was generally unstable for the dual-phase materials due to the broad nature of the peaks, strong preferred orientation and, possibly, residual stresses. Instead, estimates of volume fractions of Ag$_2$Al phase and determination of the preferred orientation were made using the 'mixture' and 'preferred orientation' functions of CRYSTALDIFFRACT (CrystalMaker Software Limited, Oxford, England). Crystal structure files from the Crystallography Open Database (http://crystallography.net/cod/browse.html) were used (entry 9013046 for Ag, entry 1502689 for Al, entry 1509011 for Ag$_2$Al).

The pore and ligament sizes were made by analyzing SEM images using IMAGEJ (https://imagej.net/ij/download.html). Fifty measurements were made of each parameter per sample.

The thin-film alloy thicknesses were measured using a XE7 Atomic Force microscope (Park Systems, Suwon, Korea). The measurements were conducted in contact mode using an NSC15 cantilever (radius of 10 nm, height of 15 μm, length of 125 μm, sensitivity of 59.99 V/μm, force constant of 40 N/m and resonance of 325 kHz according to the manufacturer). The data was collected at the edge between coated and non-coated glass substrates. The step height between a flat region and the film was measured and determined using XEI data processing and analysis software (Park Systems, Suwon, Korea).

2.3. Electrical properties of samples

The electrical resistivity measurements of np-S samples were performed using the four-probe van der Pauw method on a Hall effect measurement system (ezHEMS, NanoMagnetic Instruments, Oxford, UK) at the temperature of 300 K, a magnetic field B of 0.6268 T and a current of 1 mA. The thickness of the film is a necessary input parameter and for this we used the results of the ellipsometry (See Supplementary Material, Table S4 and Fig. S1).

As will be shown later, the sponges prepared from precursors with higher Al content had the lowest volume fraction of Ag and the finest ligaments. In addition, it has been shown previously that the classic bicontinuous fibrous sponge is best developed at active metal contents in the range of 70–80 a. % (Supansomboon et al., 2014). Therefore, it might be expected that the present sample S6 (which was prepared from a precursor composition in this range) might be expected to have highest specific surface area. The amount of the material in the samples being too small for our available BET instrument, it was decided instead to estimate the surface area of a duplicate S6 sample using electrochemical capacitance measurements, see for example Lakshmanan et al. (2015) Our method has been described elsewhere (Cortie et al., 2005) and, in brief, consists of an RC electric circuit comprising a DC power supply as a voltage source (V_s) of 1.0 V, an external resistor (R_e) of 8 kΩ, and a double pole reversing switch to the capacitor's electrodes. The latter
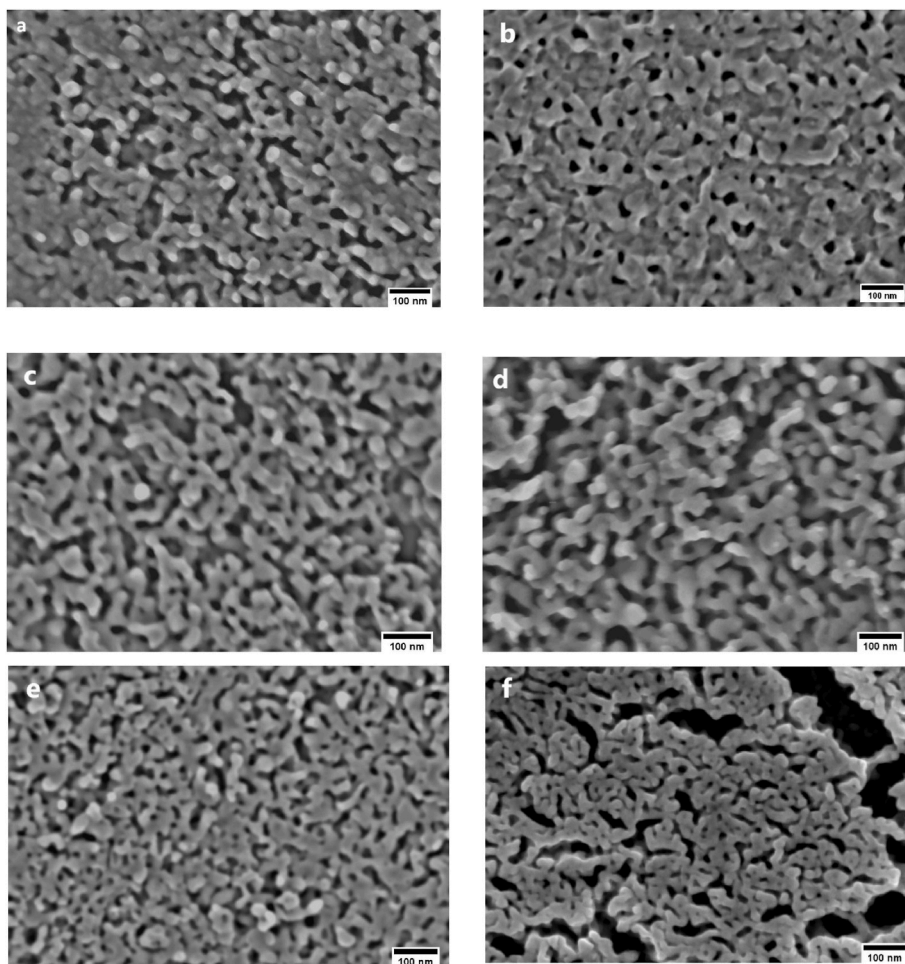
Fig. 6. Top-view SEM images of np-S samples (a) S1, (b) S2, (c) S3, (d) S4, (e) S5 and (f) S6 thin films. Prepared from as-deposited films and imaged at the same magnification (100 nm scale bar).

Table 2
Average pore and ligament sizes of as-deposited thin films dealloyed in 1 M NaOH. The confidence intervals correspond to one standard deviation. The estimated surface diffusion of Ag adatoms during the de-alloying process is also given.

	S1	S2	S3	S4	S5	S6
Average pore size, nm	12.6 ± 4.9	13.9 ± 4.4	14.4 ± 4.5	15.5 ± 4.5	11.8 ± 3.1	11.1 ± 3.5
Average ligament size, nm	31.6 ± 12.8	30.6 ± 9.8	25.3 ± 8.9	22.2 ± 8.7	15.6 ± 4.4	13.1 ± 3.9
Average pore density, pores per 10,000 nm^2	93	117	131	152	231	262
Surface diffusion of Ag D_s (m^2 s^{-1})	5.26×10^{-18}	4.96×10^{-18}	4.49×10^{-18}	3.93×10^{-18}	1.08×10^{-18}	0.72×10^{-18}

were immersed in 0.1 M KNO$_3$ aqueous electrolyte. A LabJack U12 A/D convertor was connected to the circuit to measure the voltage across the electrodes during the charge and discharge processes. The ostensible capacitance of the device can be extracted from the discharge voltage by transformation of the expression

$$V(t) = V_0 e^{-t/RC} \tag{2}$$

to

$$ln\left(\frac{V(t)}{V_0}\right) = -t/RC \tag{3}$$

where t is the elapsed time, $V(t)$ is the time-varying voltage across resistance R, and C the ostensible capacitance.

The slope $-1/RC$ was determined from least squares linear regression of data taken in incrementally advanced segments. Since the capacitance of this type of system varies with time or voltage (due to the necessity for diffusive processes in the electrical double layer or pores to occur) we chose the capacitance at 0.20 V as datum for comparison. At least 5 charge-discharge cycles were applied to a symmetrical device consist of two electrodes of S6 sponge separated by a sheet of filter paper (Fig. 1), with the device immersed in electrolyte. Capacitance was then normalized to the area of one side of a glass slide (18.75 cm^2).

2.4. Optical properties

The optical properties of the deposited thin films and the dealloyed samples were explored by ellipsometry over the range 300–2500 nm (photon energy between 4.13 and 0.496 eV) using a Variable Angle Spectroscopic Ellipsometer (VASE) (JA Woollam, Lincoln, Nebraska, USA) with a rotating polariser and a fixed analyser to measure the polarisation angles Δ and ψ. A wavelength step of 5 nm and incidence angles of 65°, 70° and 75° were used.

Spectroscopic ellipsometry is an indirect method to explore the optical properties of thin-film systems and therefore an optical model is
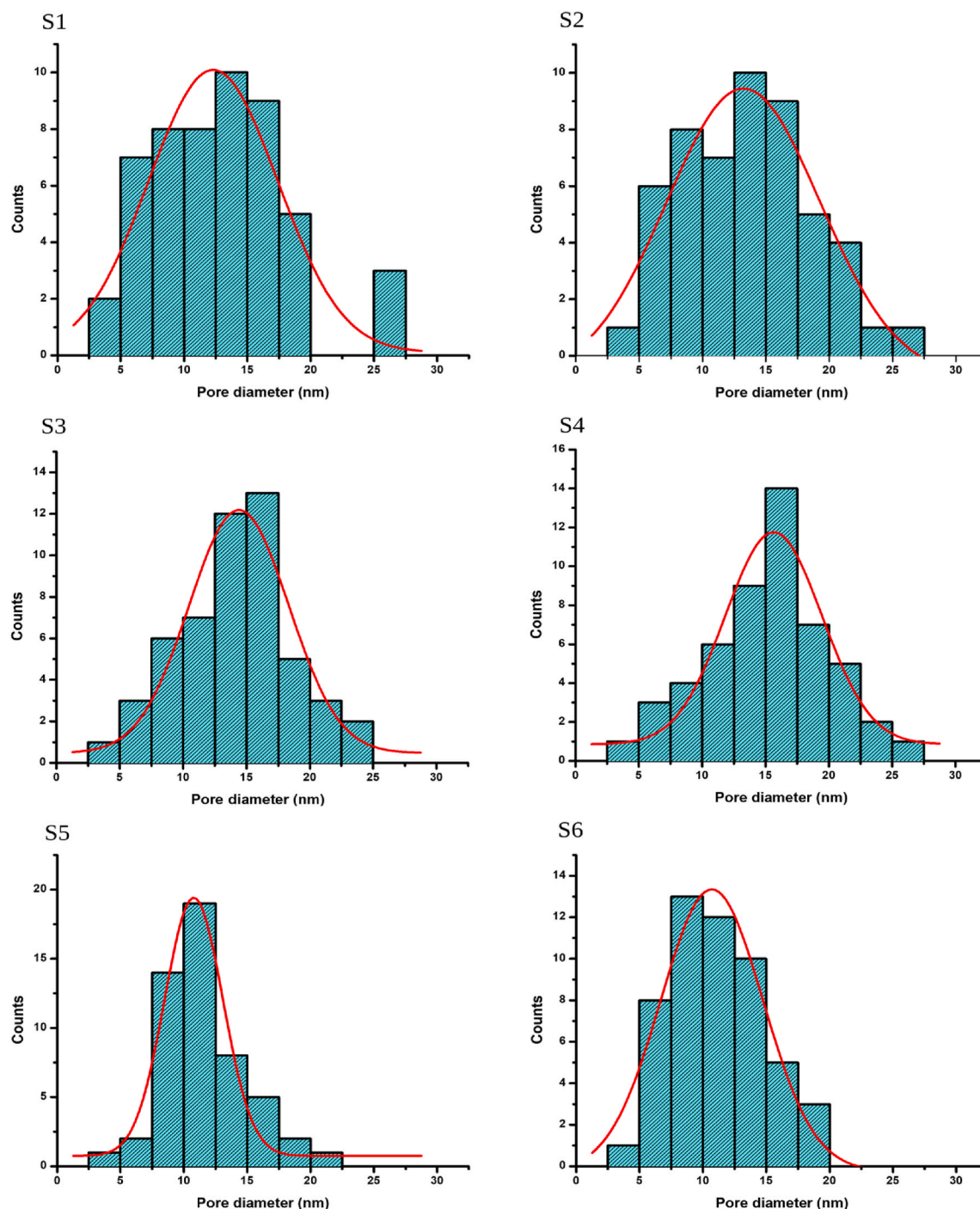
Fig. 7. Histograms of the pore diameter distribution of the np-S samples derived from the top-view SEM images.

additionally necessary to analyse the samples. Optical models were built to simulate the experimental spectra of as-deposited Ag thin films and the np-S thin films: a two-layer model consisting of an Ag alloy layer with a thickness of ~110 nm and a glass substrate layer was used for the films prior to dealloying (Fig. 2 a) whereas a three-layer model consisting of an EMA (Ag + void) layer of variable thickness, ~5 nm of TiO_2 and a glass substrate was utilised to extract the thickness and optical properties of the de-alloyed thin films (Fig. 2 b).

3. Results and discussion

In this section, the results of EDS are first introduced, then the XRD

results of deposited and dealloyed films with different Al contents are presented, and the SEM results described. Finally, the electrical properties and optical constants of the dealloyed thin films are explicitly analysed.

3.1. Composition of as-deposited and dealloyed Al_xAg_{100-x} thin-film alloys

The chemical compositions of the matrix in the $Ag_{1-x}Al_x$ thin film alloys and the corresponding sponges were obtained using EDS, Table 1. The calculated RSD is estimated to be within 1%. Dealloying of the as-deposited films was relatively complete with the residual Al content of
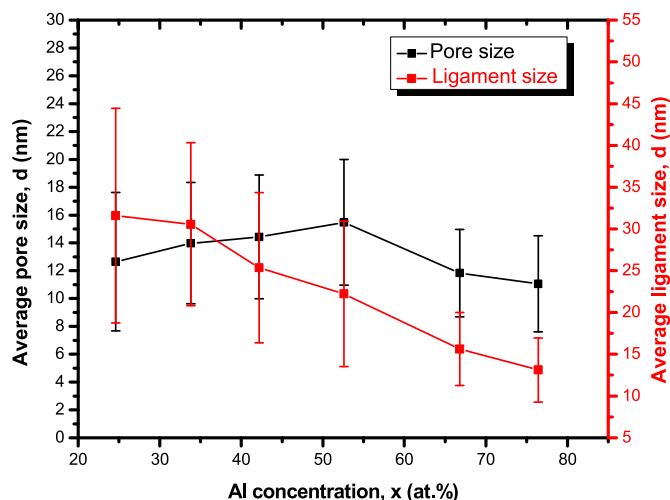
Fig. 8. Variations of the np-S ligament sizes (right) and pore sizes (left) as a function of the Al concentration in the initial alloys after dealloying in 1 M NaOH solution.
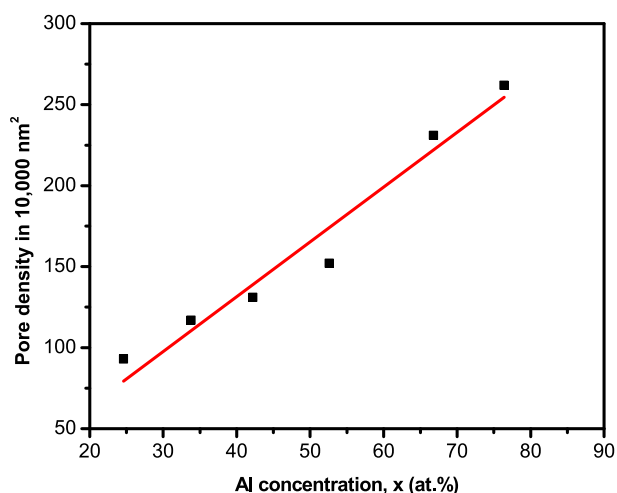
Fig. 9. Pore density as a function of Al concentration in the Al_xAg_{100-x} thin film alloys. The red line is the best linear fit for the data. (For interpretation of the references to colour in this figure legend, the reader is referred to the Web version of this article.)

the np-S lying into the range 1.4–5.9 at.%. Residual Al at these levels has been reported in np-S by past workers too (Yamauchi et al., 2003; Wang et al., 2009). It is evident that the as-deposited samples were all dealloyed, even, surprisingly, those with Al contents well below the 50 at.% or so of the traditional 'parting limit' (Supansomboon et al., 2014). This is not the case for the annealed samples, which hardly de-alloyed. This is evidently due, for the most part, to the formation of additional Ag_2Al phase in those samples (see next section). The Ag_2Al phase is well known to be resistant to corrosion in NaOH solutions (Yamauchi et al., 2003; Luo et al., 2020). Apparently, the relatively defective and metastable structure of the as-deposited films renders them very susceptible to dealloying. The Al contents of the deposited surfaces are also marginally higher after annealing. We attribute this to some Al_2O_3 having been formed on the exposed surfaces of the films despite annealing having been conducted under reducing conditions. The corollary to this is that the Ag content immediately below the surface would be enriched relative to the content of metallic Al.
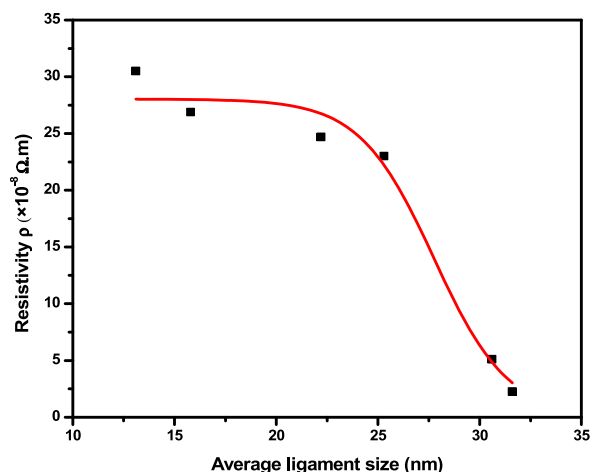
Fig. 10. The electrical resistivity change versus the average ligament size of the np-S thin films, the curve indicates that the electrical resistivity of the sponges increases with decreasing the average ligament size.

Table 3
Carrier concentration, Hall mobility and electrical resistivity of np-S thin films deposited on glass substrate with different pore and ligament diameters.

	Carrier concentration (m^{-3})	Hall mobility (m^2. V^{-1}s^{-1})	Electrical resistivity (Ω.m)
S1	1.5×10^{29}	1.6×10^{-3}	2.26×10^{-8}
S2	1.9×10^{29}	1.2×10^{-3}	5.10×10^{-8}
S3	2.1×10^{29}	1.3×10^{-4}	2.30×10^{-7}
S4	2.4×10^{29}	1.0×10^{-4}	2.47×10^{-7}
S5	2.6×10^{29}	8.9×10^{-5}	2.69×10^{-7}
S6	2.9×10^{29}	3.2×10^{-5}	3.05×10^{-7}

3.2. Phase constitution of the $Ag_{1-x}Al_x$ thin-film alloys and dealloyed thin films

3.2.1. As-deposited then dealloyed

Fig. 3a shows the XRD patterns of these films in the as-deposited condition. The patterns reveal that, with a low concentration of Al (24.6 atom %) (sample S1), there is a single phase – the solid solution α-Ag(Al) face-centred cubic crystal structure – with space group $Fm\overline{3}m$. This phase shows a weak (111) texture. This is despite the fact that the binary equilibrium phase diagram for Ag–Al shows that Ag_2Al phase should have formed (Murray, 2016). Evidently, a metastable solid solution of (Ag,Al) formed instead. This is a common occurrence for magnetron sputtering at ambient temperature; there is often insufficient thermal activation of diffusive processes to crystallise complex intermetallic structures and so simple metastable closest-packed phases form instead. A transition in microstructure was observed at Al of 33.8 atom % (sample S2), where δ-Ag_2Al intermetallic compound with hexagonal primitive structure and space group of P63/mmc started to form, resulting in a mixture of two phases, namely α-Ag(Al) and δ-Ag_2Al. The Ag_2Al usually had a strong (002) texture, but the (101), (012), (103), (112) and (004) peaks are usually also visible in the patterns for samples S2 through to S4. According to the XRD results, with increase of Al content from 33.8 to 52.6 at.%, the amount of α-(Ag,Al) decreases while that of Ag_2Al increases as indicated by the variation of diffraction peak intensities of these phases. This is as expected from the binary phase diagram of this system. Nevertheless, an examination of the binary phase diagram shows that far more Ag_2Al phase *should* have formed, so evidently the deposit is still in a relatively metastable condition. At high Al concentrations of 62.2 and 72.6 atom % (samples S5 and S6), the XRD peaks show only diffraction peaks associated with a single face-centred cubic (fcc), in this case Al-rich α-(Al,Ag) phase solid solution. This result
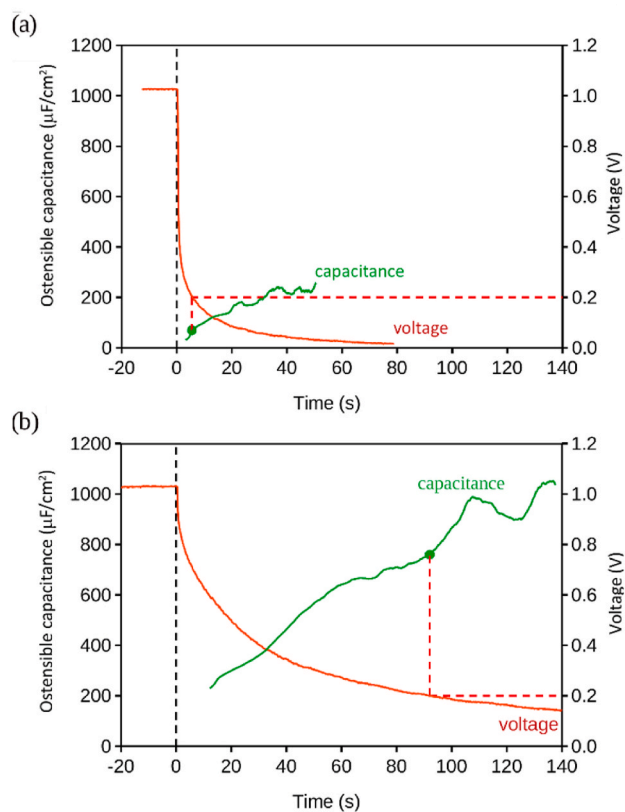
Fig. 11. Discharge voltages and electrochemical capacitances of (a) as-deposited Ag-75.at% Al film, and (b) np-S produced from the above film by de-alloying in NaOH. The capacitances vary with voltage and time and are compared at a datum of 0.20 V (dashed lines).

for 72.6 at.% Al is in good agreement with the results of Yang et al. (2013) for their $Ag_{28}Al_{72}$ thin film prepared using a magnetron sputtering system. Although the binary phase diagram predicts some Ag_2Al for lower temperatures, it will be noted that Ag is extremely soluble in fcc(Al) at elevated temperatures. The absence of Ag_2Al in these samples may therefore be attributed to insufficient thermal activation being available at time of deposition.

The progressive shift of the most intense (111) diffraction peak with 2θ at different concentrations of Al is displayed in Fig. 3b. The (111) peaks of the alloys shift towards the higher angle with increasing Al concentration. The lattice parameters of these thin films ranged systematically between 0.4081 ± 0.0002 nm at the lowest Al content to 0.4042 ± 0.0002 nm at the highest Al content, which corresponds to the reported values of Ag (0.40790 nm) and Al (0.40406 nm) in the Crystallography Open Database's entries ID no. 9011607 and 9012956, respectively. The measured lattice parameter values have been plotted against Al concentrations in Fig. 4. The lattice parameter (a_0) decreases with increasing Al concentration, showing a not-quite linear relationship that is only in poor agreement with Vegard's law. The results indicate that when the Al composition is less than 40 at.%, it is the α-Ag (Al) solid solution that is dominant whereas the α-Al(Ag) solid solution exists with Al composition higher than 60 at.%. A metastable (Ag,Al) α phase exists between roughly 40 and 60 at.% Al.

Rietveld refinement of the fractions of Ag and Ag_2Al phases present was unstable due to the strong texture of the films and the broad nature of the peaks from these thin films. Instead, we used CRYSTALDIFFRACT's 'mixture' and 'preferred orientation' functions to estimate the amount of Ag_2Al phase (balance usually being fcc (Ag,Al) or (Al,Ag) phases). These results are also shown in Table 1. For comparison, the maximum amount of Ag_2Al that could possibly form for the measured Al contents and from

the published binary equilibrium diagram [50] is also listed using 500 °C as a datum.

The XRD patterns of the samples dealloyed in 1 M NaOH solution (Fig. 5) generally showed only fcc (Ag,Al) solid solution, although there was also evidence for a small proportion of retained Ag_2Al in some patterns of samples S3 and S5. It is evident that Al can be mostly, but not entirely, leached out using NaOH solution as a result of the significant difference in electrode potential Ag and Al. This is notwithstanding the known corrosion resistance of Ag_2Al in NaOH solutions and despite the fact that samples S1 to S3 had Al contents below the traditional parting limit. The lattice parameters of these np-S thin films were 0.40810 ± 0.00020 nm. This is within the range of values reported for pure Ag (*cf.* the COD entry no. 9011607).

3.2.2. As-deposited, annealed at 500 °C, then dealloyed

A duplicate of each as-deposited sample was annealed at 500 °C to see whether this would affect the morphology of the subsequent sponge. From Table 1 it is clear that annealing of the as-deposited films caused a marked increase in the fraction of Ag_2Al. In samples S1, S2 and S3 this is likely the consequence of much of the Al in the as-deposited material having originally being in metastable solid solution in the fcc(Ag,Al) phase. Annealing provided the thermal activation necessary to precipitate out an amount of Ag_2Al that was closer to the equilibrium situation at 500 °C. However, the amount of Ag_2Al estimated for samples S4, S5 and S6 was far above that predicted from the equilibrium phase diagram for the measured compositions of the films. The reason for anomalously strong XRD peaks of Ag_2Al in these samples is unknown but the phenomenon may be related to the preferred orientation being stronger than assumed and/or the fact that some of the Al had oxidized thereby enriching the ratio of Ag to metallic Al. Annealed sample S6 showed a very strong 201 texture of Ag_2Al, which was unusual. Overall, the content of annealed Ag_2Al also made these films much more resistant to dealloying with the result that they still contained appreciable amounts of Al after treatment in NaOH solution. Sample S2 also appeared to also contain some $Al(OH)_3$ or other third phase that had evidently formed during dealloying (peaks at d = 4.00, 3.48, 3.10 and 2.83 Å). The XRD patterns of these films are shown in the Supplementary Material, Fig. S2.)

3.3. Effect of composition in the $Ag_{1-x}Al_x$ precursor alloys on the morphology of np-S

The effect of the Al content of the precursor on the morphology of np-S seems controversial. For example, Yamauchi et al. (2003) reported that there was little effect of varying the Al between 61 and 85 at.%. In contrast, Wang et al. (2009) and Song et al. (2011) reported a significant decrease in ligament size as Al was increased. Plane-view SEM images of some example regions of the present np-S are shown in Fig. 6. The thin films produced by dealloying as-deposited material all have bi-continuous spongy structures with nanoscale open-cell pores and silver ligaments. As can be seen from these images, when the concentration of the deposited Al was low (24.6 at.%, sample S1), the sponge formed had pits distributed sparsely and randomly on the surface (Fig. 6a). Further increasing the concentration of Al in the $Ag_{1-x}Al_x$ thin film alloy brought in an appreciable change in the ligament sizes (Fig. 6 b, c, d, e and f). There was less effect on the pore size. The mean average sizes of the ligaments and pores are summarised in Table 2. The ligament sizes are significantly smaller than the 90–450 nm and 140–330 nm reported for melt-spun ribbon precursors by Wang et al., 2009 and Song et al. (2011) respectively. The thickness of the as-deposited films was measured using atomic force microscopy and fell with the range 118–121 nm (Supplementary Materials, Fig. S3).

Figs. 7 and 8, and Table 2, show the pore sizes for the np-S samples. As summarised in Fig. 8, increasing the Al concentration in the initial alloys led to a linear decrease in the average ligament size and a linear increase in the average pore size of the resulting np-S which peaked at
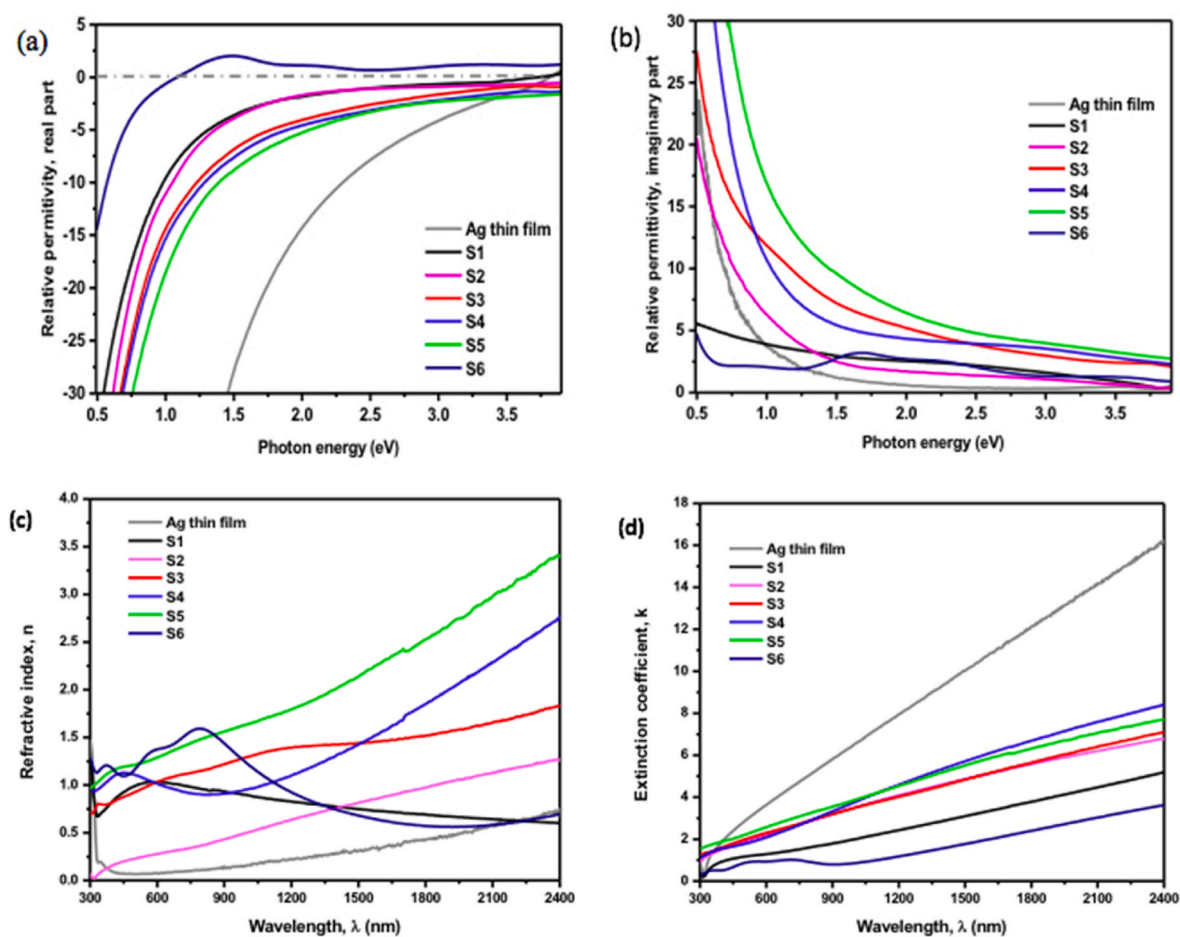
Fig. 12. Measured data of (a) the real part of the complex dielectric function of the np-S samples with the different average ligament sizes, (b) the imaginary part of the complex dielectric function of the np-S samples with the different average ligament sizes, and the optical constants of (c) the refractive index and (d) the extinction coefficient as a function of wavelength.. (This data is for the as-deposited then de-alloyed samples. The curves for solid Ag are shown for interest but are not directly comparable to the data for the sponges.)

52.6 at.% Al (S4). Density of pores is shown in Fig. 9 and Table 2.

Ligament size has been shown to be related to the rate of surface diffusion of the noble metal alloys during dealloying (Ji et al., 2011; Yang et al., 2019). The latter can be estimated using Eq. (4):

$$D_s = \frac{[d(t)]^4 kT}{32\, \gamma t a^4} \qquad (4)$$

where $d(t)$ is the average size of ligaments at the dealloying time t in nm, k is the Boltzmann constant (1.3086×10^{-23} J K^{-1}), T is the temperature during the dealloying process (298 K), γ is the Ag surface energy (1.302 J m^{-2}), t is dealloying time in seconds, and a is the Ag lattice parameter (0.4086 nm). The results in Table 2 demonstrate that the average ligament sizes of np-S and the calculated surface diffusion D_s (Eq. (4)) of Ag adatoms depend on the Al content in the precursors. Increasing the Al concentration from 24.6 to 72.6 at.% led to a decrease in the ligament sizes from 31.6 ± 12.8 to 13.1 ± 3.9 nm, which may be attributed to lowering the surface diffusion of Ag adatoms along alloy/electrolyte interfaces from 5.26×10^{-18} to 0.72×10^{-18} m^2 s^{-1} and hence stabilising the np-S structure in the dealloying process. These results of D_s presented in Table 2 are about two orders of magnitude lower than the value (10^{-16} m^2 s^{-1}) of the surface diffusion of Ag adatoms prepared by dealloying of Ag–Al alloys at 363 K in H$_2$SO$_4$, H$_3$PO$_4$, C$_2$H$_2$O$_4$ and HCl solutions reported by Song and co-workers (Song et al., 2011). Moreover, the calculated values in Table 2 are significantly higher than the intrinsic surface diffusion coefficients of Ag value (10^{-20} m^2 s^{-1}) by about 2 orders of magnitude (Li et al., 2017).

As mentioned earlier, the films that had been annealed before dealloying did not substantially dealloy, although their surface regions were certainly partially etched. These samples therefore are not yet converted to np-S although they could presumably be rendered into that state by more aggressive etching, as for example by HCl which is known to attack Ag$_2$Al (Luo et al., 2020).

3.4. Electrical resistivity of the NP-S thin films with different ligament sizes

It has been reported that the electrical resistivity of nano-porous materials depends on their morphology (Fujita et al., 2008; Zuruzi and Siow, 2015). The dealloyed nanoporous materials have a bicontinuous structure, where the nanoscale ligaments create interconnected networks that function as efficient channels for electron conduction. The electrical resistivity of the np-S thin films can be directly correlated with the average ligament size and hence, indirectly, the Al content in the precursor as Fig. 10. The high-resolution SEM images in Fig. 6 show that the np-S ligaments are fully percolated (connected) across the samples, providing conduction paths for electron transportation. Therefore, all the dealloyed Ag$_{1-x}$Al$_x$ samples formed conductive np-S thin films. However, we noted that the resistivities of the np-S thin films are higher than the resistivity of a Ag thin film comparator (1.32×10^{-8} Ωm, which is very similar to the value of 1.59×10^{-8} Ωm reported for bulk Ag (Fuller et al., 2002)). The identical finding has been documented by Zhang and his colleagues (Zhang et al., 2009). They found that
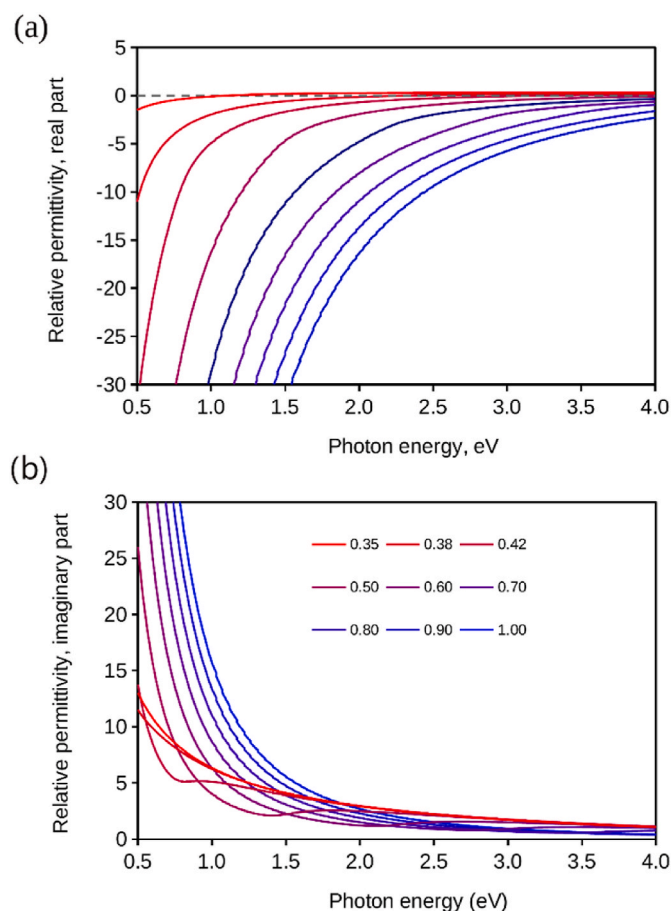
Fig. 13. Relative permittivity of sponges comprised of various volume fractions of Ag-6.5 at.% as calculated from the Bruggeman effective medium equation. Note that the form of the experimental data for samples S1 and S6 is qualitatively reproduced in these simulations when low volume fractions of metal are used.
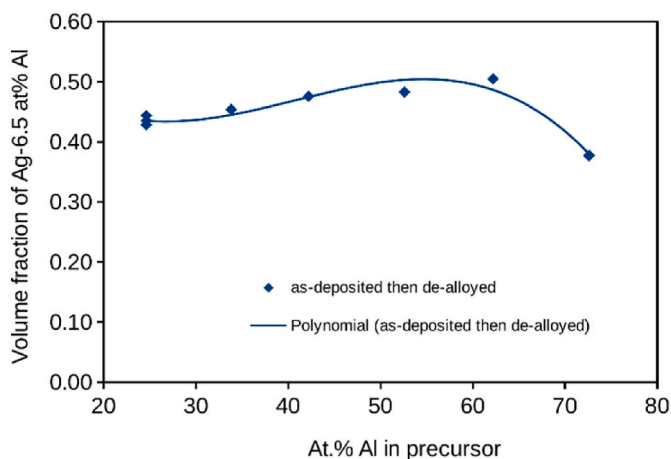
Fig. 14. Volume fractions of metal in the experimental sponges estimated from the real part of their permittivities using a Bruggeman model comprised of the Ag-6.5 at.% Al and voids.

nanoporous ribbons of gold (NPG), silver (NPS), and copper (NPC) had electrical resistivities that were ten to one hundred times higher than those of the bulk materials. This was attributed to the unique mechanism of the electron transport process in nanoporous metals.

It is well known that the presence of pores with sizes below the

electron mean free path, which is roughly 57 nm at room temperature (Doremus, 2002), would have an impact on the conduction mechanism in the silver film. Fig. 10 indicates that the electrical resistivity of np-S increases with a decrease in the average ligament size. The np-S with 31.6 nm ligament size (S1) was ten times more conductive ($\rho = 2.26 \times 10^{-8}$ Ωm) than the np-S thin films with average sizes of 25.3 (S3), 22.2 (S4), 15.6 (S5), and 13.1 (S6), with their measured electrical resistivities being 2.30×10^{-7}, 2.47×10^{-7}, 2.69×10^{-7}, and 3.05×10^{-7} Ωm respectively. The resistivity (5.10×10^{-8} Ωm) of np-S with an average ligament size of 30.6 nm (S2) was anomalously high and can probably be discarded as an outlier. The electrical resistivity of np-S thin films goes up as the diameter of the ligaments goes down. This is because electrons scatter strongly at the points where pores and ligaments meet, and this scattering gets worse as microstructural features get smaller. This then leads to greater resistance (Fujita et al., 2008). The Hall mobility of the charge carriers in np-S with a ligament diameter of 31.6 nm is two orders of magnitude higher than that of np-S with a ligament diameter of 13.1 nm. This is true even though the carrier density of the np-S remained relatively unchanged with the diameter of the silver ligaments, as Table 3 shows.

According to Hakamada and his colleagues' research (Hakamada et al., 2016), the electrical resistivity of nanoporous gold (np-G) increases as the size of the ligaments decreases. Additionally, np-G thin films with nanostructure parameters close to the dimensions of np-S in this study exhibit higher electrical resistivity. The electrical resistivity of np-G thin films with ligament sizes of 77, 24, and 23 nm is 2.46×10^{-7}, 4.26×10^{-7}, and 5.48×10^{-7} Ωm, respectively. However, the measured electrical resistivity of np-S with the small ligament sizes is analogous to the findings by Stewart et al. (2017) for np-S prepared by sintering Ag nanowires at 300° C to eliminate the junction resistance between nanowires in a network. The electrical resistivity of the resulting porous structure prepared by melting the AgNWs with 6.2 μm in length and 48 nm in diameter was 2.00×10^{-7} Ωm and for the nanoporous formed by sintering the AgNWs with 27 μm in length and 150 nm in diameter was 2.74×10^{-7} Ωm. Moreover, the electrical resistivity of the interconnected network of particles formed by sintering the AgNPs was 2.93×10^{-7} Ωm.

3.5. Electrochemical capacitance as an indicator of specific surface area

The capacitance of the as-deposited Ag-75at.% Al alloy thin film (S6) and then the np-S produced from it were experimentally obtained from discharge curves of symmetric electrodes in 0.1 M KNO$_3$ aqueous electrolyte, Fig. 11. As-deposited Ag-75 at% Al thin film alloy (similar to S6) had a capacitance of 67 μF cm^{-2} (sd = 21 μF cm^{-2}, $n = 6$) at 0.20 V in 0.1 M KNO$_3$ solution. In contrast, after dealloying, the subsequent np-S thin film had a capacitance of 665 μF cm^{-2} (sd = 124 μF cm^{-2}, $n = 15$). Therefore, it is evident that the surface area of this sponge is about ten times larger than its starting film from an electrochemical perspective.

3.6. Optical properties of the NP-S thin films as an indicator of morphology

Further insight into the structure of the dealloyed films was obtained from an analysis of their optical properties.

3.6.1. Dielectric permittivity

The frequency-dependent dielectric permittivity $\varepsilon(\omega)$ for non-magnetic materials is expressed as (De Silva et al., 2017):

$$\varepsilon(\omega) = \varepsilon_1(\omega) + i\varepsilon_2(\omega) \qquad (5)$$

where ω is the frequency of the light, and ε_1 and ε_2 are the real and imaginary parts of the permittivity respectively. The permittivities of the dealloyed films were extracted from the ellipsometry data as described in the experimental section, and are plotted in Fig. 12 a and b, which

shows the real (ε_1) and imaginary (ε_2) dielectric permittivity of the samples. In this type of analysis, the sponges are conceptually treated as new materials in their own right, with effective permittivities that differ from that of solid Ag. Essentially, the nanocomposite material is being treated as a 'metamaterial' (Maaroof et al., 2007), albeit a rather simple one. In general, the real and imaginary components of the dielectric permittivity of the nano-plasmonic materials are the fundamental consideration when evaluating the optical and plasmonic properties (Cortie et al., 2019; Arnold and Blaber, 2009) of a material. It is worth noting that the real component of the permittivity determines the resonance frequency, which would be operating point for many devices that exploit the optical properties. The imaginary component (ε_2) of the dielectric permittivity is associated with the optical losses which arise from interband transition, intraband transition (Erwin et al., 2016), and electron surface scattering caused by grain boundaries (West et al., 2010), surface roughness (Sardana et al., 2014), lattice defects (West et al., 2010) and porosity (Sardana et al., 2014).

Inspection of Fig. 12 a and b shows that the curves for the real part of permittivity are spread over a broad range but all samples are less metallic than the pure Ag comparator. The curves of samples S2 to S5 do not fall in a sequence however and are all rather similar in magnitude. The situation for the complex part of the permittivity is even more irregular. Samples S2 to S5 have a complex permittivity that is more positive than that of pure Ag, attesting to the considerable electron scattering in these sponges. In contrast, samples S1 and S6 showed a lower magnitude of ε_2 at low photon energies. Importantly, the optical properties are also strongly affected by volume fraction of solid material, a factor that we will investigate below using an 'effective medium model' (EMA).

When the characteristic size of the constituents of the material is small compared to the wavelength of the light in the media, as is the case for the present sponges, their optical response can be formulated by effective medium approximations. In these approximations, the dielectric functions of the constituents that make up the composite material are combined in an analytical relation that provides an estimate of the effective dielectric constant of the material under investigation (Garoli et al., 2018). Many EMAs have been proposed but the Bruggeman EMA is the most popular approach to obtaining the permittivity of mixed-phase films of the present type. This EMA has been exploited, for example, for the computation of the optical properties of nanoporous gold by Maaroof et al. (2005), with the practise being subsequently taken up for np-S by some subsequent workers, e.g. (Garoli et al., 2018; Detsi et al., 2014). Here we used this EMA to simulate the permittivity of sponges with varying volume fractions of metal phase, Fig. 13. We chose to use permittivity data for Ag-6.5 at% Al for the metal phase as that composition was broadly representative of the np-S. The similarity in form to the experimental data is striking even if the ε_2 values of the experimental data are somewhat higher at low photon energies. Note especially that, at low volume fractions of metal, the simulation reproduces the anomalous shape of the curves for samples S1 and S6 thereby indicating that these two samples have lower volume fraction of metal than the others. We also estimated the porosity by optimizing the volume fraction of each sample against its ε_1 curve using the Bruggeman EMA. (The ε_2 curves of the sponges evidently contain additional scatter and extinction beyond that present in the thin film of the reference Ag-6.5 at.% Al sample so was not suitable for fitting against.) It was also observed that use in the Bruggeman model of the dielectric function for Al-6.5 at% Ag from de Silva et al. (De Silva et al., 2017) produced a much better fit than use of the dielectric function for pure Ag (an average least square deviation of 1.7 relative permittivity units vs 2.7 respectively). This supports the observation that the metallic portion on these sponges is Ag–Al alloy rather than pure Ag. The estimated volume fractions of Ag in each sponge are plotted in Fig. 14. Sample S6, produced from the most Al-rich precursor has the lowest volume fraction, but the analysis indicates that all the samples have metallic volume fractions are broadly in the range of 0.4–0.5, with those of S1 and S6

being the lowest. This independently corroborates the unusual form of the ε_2 curves of S1 and S6 which can only be reproduced in the model by using relatively low volume fractions of metal.

3.6.2. Optical constants

These extracted values are presented in Fig. 12 c and d. The optical constants are commonly described using a complex equation:

$$M(\lambda) = n(\lambda) + ik(\lambda) \tag{6}$$

The real component, n, is typically known as the refractive index of the material which governs a wave's phase shift and velocity as it travels through the material. The imaginary component, k, is referred to as the extinction coefficient and is responsible for determining the attenuation of the amplitude of the wave (Losic and Santos, 2015; Maaroof et al., 2005). Nanoporous materials can be characterised as a composite of dense materials and air. As a result, their refractive indices are determined by both the degree of porosity as well as the refractive indices of the dense materials (ligaments) (Knez, 2019; Losic and Santos, 2015).

It is apparent in Fig. 12 c that refractive indices of all of the np-S thin films were larger than those of the Ag thin film in the wavelength range from 350 nm to 2250 nm. This is because the Ag thin film has a very low refractive index in this range – less than 1 – which is characteristic of metal behaviour. The refractive indices of the np-S thin films do not follow a consistent pattern at the lower wavelength range from 300 to 1500 nm. Nevertheless, S2 shows a refractive index that is almost identical to zero at wavelengths that are less than 350 nm, while S6 shows the highest refractive index value at this wavelength range, which follows from its almost insulator-like behaviour. On the other hand, when the wavelength was greater than 1500 nm, S2 to S5 show high refractive indices values and exhibited a relatively less metallic behaviour.

Fig. 12 d shows that the extinction coefficient values of the np-S thin films and Ag thin film increase noticeably with wavelength of the incident beam. Nonetheless, the extinction coefficients of the np-S thin films still show much lower values than those of the Ag thin film. This is due to the Drude free electron response of Ag which is more developed in the Ag thin film than in the sponges. As a result, the relative attenuation of the np-S thin films and the Ag thin film diverges dramatically as the wavelength increases.

4. Conclusions

The morphology of nanoporous silver made by dealloying with 1M NaOH solution can be controlled by varying the Al content of precursor thin films. In general, the structure becomes finer for greater starting Al contents. Average ligament size can be tuned from about 32 to 13 nm by increasing the Al content in the precursor from 25 to 73 at.%. In contrast, pore size itself is not dramatically changed. The density of the pores, in contrast, increases markedly as the Al content in the precursor increases. Measurement of the electrochemical capacitance showed that the sponge produced from a precursor containing 75 at.% Al had a surface area that was an order of magnitude greater than its starting thin film.

The electrical resistivity increases with increase in initial Al content. This is evidently due to a combination of finer ligament size and greater pore density. The volume fraction of metal can be estimated by analysis of the optical properties of the sponges. Specifically, spectroscopic ellipsometry was used to extract a relative dielectric permittivity of each sponge, and the results for the real part of permittivity matched to a volume fraction estimated by use of the Bruggeman effective medium model, using a nanocomposite comprised of variable volume fractions of Ag-6.5 at.% Al and air.

Annealing of the films prior to dealloying was not helpful. Annealing increased the amount of the corrosion resistant Ag_2Al phase, evidently due to the formation of some Al_2O_3 and consequent enrichment of Ag content in the sub-surface film. In contrast, dealloying of the as-

deposited films was rapid and effective, even at Al contents well below the traditional parting limit. This is likely due to the profusion of atomic-scale structural defects in the as-deposited film which render it relatively susceptible to corrosion.

In conclusion, we have shown that dealloying of magnetron sputtered thin films is a convenient method to produce nano-porous silver sponges with controlled morphologies, electrical and optical properties.

CRediT authorship contribution statement

Sanaa A. Alzahrani: Writing – original draft, Methodology, Investigation, Formal analysis, Data curation, Conceptualization. **Kaludewa S.B. De Silva:** Writing – review & editing, Supervision, Methodology, Conceptualization. **Annette Dowd:** Writing – review & editing, Supervision, Project administration, Methodology, Conceptualization. **Matthew D. Arnold:** Validation, Supervision, Methodology, Investigation. **Michael B. Cortie:** Writing – review & editing, Supervision, Resources, Methodology, Investigation, Formal analysis, Conceptualization.

Declaration of competing interest

The authors declare that they have no known competing financial interests or personal relationships that could have appeared to influence the work reported in this paper.

Data availability

Data will be made available on request.

5. Acknowledgements

Appendix A. Supplementary data

Supplementary data to this article can be found online at https://doi.org/10.1016/j.rsurfi.2024.100217.

References

Abednatanzi, S., Abbasi, A., Masteri-Farahani, M., 2015. Enhanced catalytic activity of nanoporous Cu 3 (BTC) 2 metal–organic framework via immobilization of oxodiperoxo molybdenum complex. New J. Chem. 39, 5322–5328. https://doi.org/10.1039/C5NJ00618J.
Arnold, M.D., Blaber, M.G., 2009. Optical performance and metallic absorption in nanoplasmonic systems. Opt Express 17, 3835–3847.
Cortie, M.B., Arnold, M.D., Keast, V.J., 2019. Quest for zero loss : unconventional materials for plasmonics. Adv. Mater. 32, 1904532 https://doi.org/10.1002/adma.201904532.
Cortie, M.B., Maaroof, A.I., Smith, G.B., 2005. Electrochemical capacitance of mesoporous gold. Gold Bull. 38, 15–23. https://doi.org/10.1007/BF03215223.
Cortie, M.B., Maaroof, A.I., Stokes, N., Mortari, A., 2007. Mesoporous gold sponge. Aust. J. Chem. 60, 524–527. https://doi.org/10.1071/CH06372.
DE Silva, K.S., Keast, V.J., Gentle, A., Cortie, M.B., 2017. Optical properties and oxidation of α-phase Ag–Al thin films. Nanotechnology 28, 095202. https://doi.org/10.1088/1361-6528/aa5782.
Detsi, E., Salverda, M., Onck, P.R., DE Hosson, J.T.M., 2014. On the localized surface plasmon resonance modes in nanoporous gold films. J. Appl. Phys. 115, 044308 https://doi.org/10.1063/1.4862440.
Detsi, E., Sellès, M.S., Onck, P.R., DE Hosson, J.T.M., 2013. Nanoporous silver as electrochemical actuator. Scripta Mater. 69, 195–198. https://doi.org/10.1016/j.scriptamat.2013.04.003.
Detsi, E., Vuković, Z., Punzhin, S., Bronsveld, P.M., Onck, P.R., DE Hosson, J.T.M., 2012. Fine-tuning the feature size of nanoporous silver. CrystEngComm 14, 5402–5406. https://doi.org/10.1039/C2CE25313E.
Ding, Y., Zhang, Z., 2016. Nanoporous Metals for Advanced Energy Technologies. Springer.
Doremus, R.H., 2002. Optical properties of small clusters of silver and gold atoms. Langmuir 18, 2436–2437.
Erlebacher, J., Aziz, M.J., Karma, A., Dimitrov, N., Sieradzki, K., 2001. Evolution of nanoporosity in dealloying. Nature 410. https://doi.org/10.1038/35068529, 450-435.
Erwin, W.R., Zarick, H.F., Talbert, E.M., Bardhan, R., 2016. Light trapping in mesoporous solar cells with plasmonic nanostructures. Energy Environ. Sci. 9, 1577–1601. https://doi.org/10.1039/C5EE03847B.
Forty, A.J., 1979. Corrosion micromorphology of noble metal alloys and depletion gilding. Nature 282, 597–598. https://doi.org/10.1038/282597a0.
Fujita, T., Okada, H., Koyama, K., Watanabe, K., Maekawa, S., Chen, M., 2008. Unusually small electrical resistance of three-dimensional nanoporous gold in external magnetic fields. Phys. Rev. Lett. 101, 166601 https://doi.org/10.1103/PhysRevLett.101.166601.
Fuller, S.B., Wilhelm, E.J., Jacobson, J.M., 2002. Ink-jet printed nanoparticle microelectromechanical systems. J. Microelectromech. Syst. 11, 54–60.
Garoli, D., Calandrini, E., Bozzola, A., Toma, A., Cattarin, S., Ortolani, M., DE Angelis, F., 2018. Fractal-like plasmonic metamaterial with a tailorable plasma frequency in the near-infrared. ACS Photonics 5, 3408–3414. https://doi.org/10.1021/acsphotonics.8b00676.
Haber, J., 1991. Manual on catalyst characterization (Recommendations 1991). Pure Appl. Chem. 63, 1227–1246. https://doi.org/10.1351/pac199163091227.
Hakamada, M., Kato, N., Miyazawa, N., Mabuchi, M., 2016. Water-adsorption effect on electrical resistivity of nanoporous gold. Scripta Mater. 123, 30–33.
Hakamada, M., Mabuchi, M., 2009. Preparation of nanoporous Ni and Ni–Cu by dealloying of rolled Ni–Mn and Ni–Cu–Mn alloys. J. Alloys Compd. 485, 583–587. https://doi.org/10.1016/j.jallcom.2009.06.031.
Ji, H., Wang, X., Zhao, C., Zhang, C., Xu, J., Zhang, Z., 2011. Formation, control and functionalization of nanoporous silver through changing dealloying media and elemental doping. CrystEngComm 13, 2617–2628. https://doi.org/10.1039/C0CE00900H.
Jiang, Z., Jiang, D., Hossain, A.S., Qian, K., Xie, J., 2015. In situ synthesis of silver supported nanoporous iron oxide microbox hybrids from metal–organic frameworks and their catalytic application in p-nitrophenol reduction. Phys. Chem. Chem. Phys. 17, 2550–2559. https://doi.org/10.1039/C4CP04594G.
Knez, M., 2019. World scientific reference of hybrid materials. World Scientific (In 3 Volumes) 1, 166–202.
Kurowska-Tabor, E., Gawlak, K., Hnida, K., Jaskuła, M., Sulka, G.D., 2016. Synthesis of porous thin silver films and their application for hydrogen peroxide sensing. Electrochim. Acta 213, 811–821. https://doi.org/10.1016/j.electacta.2016.08.007.
Lakshmanan, C., Viswanath, R.N., Polaki, S.R., Rajaraman, R., Dash, S., Tyagi, A.K., 2015. Surface area of nanoporous gold: effect on temperature. Electrchimica Acta 182, 565–572. https://doi.org/10.1016/j.electacta.2015.09.104.
Li, B., Li, M., Zeng, Q., Wu, X., 2016a. Monolithic nanoporous copper fabricated through decomposition and sintering of oxalate. Micro & Nano Lett. 11, 378–381. https://doi.org/10.1049/mnl.2016.0034.
Li, C., Zhang, T., Zhang, M., Jin, Y., Zuo, L., Xu, H., Li, R., 2017. Fabrication of fine spongy nanoporous Ag-Au alloys with improved catalysis properties. Prog. Nat. Sci.: Mater. Int. 27, 658–663. https://doi.org/10.1016/j.pnsc.2017.05.002.
Li, R., Liu, X., Wang, H., Zhou, D., Wu, Y., Lu, Z., 2016b. Formation mechanism and characterization of nanoporous silver with tunable porosity and promising capacitive performance by chemical dealloying of glassy precursor. Acta Mater. 105, 367–377. https://doi.org/10.1016/j.actamat.2015.12.042.
Li, W., Lv, S., Wang, Y., Zhang, L., Cui, X., 2019. Nanoporous gold induced vertically standing 2D NiCo bimetal-organic framework nanosheets for non-enzymatic glucose biosensing. Sensor. Actuator. B Chem. 281, 652–658. https://doi.org/10.1016/j.snb.2018.10.150.
Li, Z., Lu, X., Qin, Z., 2013. Formation of nanoporous silver by dealloying Ag22Zn78 alloy at low temperature in H2SO4. Int. J. Electrochem. Sci. 8, 3564–3571. https://doi.org/10.1016/S1452-3981(23)14412-9.
Liu, Y., Huang, J., Wang, X., Tsai, M., Wang, Z., 2018. Nanoporous foam fabricated by dealloying AgAl thin film through supercritical fluid corrosion. RSC advances 8, 13075–13082. https://doi.org/10.1039/C8RA00463C.
Losic, D., Santos, A., 2015. Electrochemically Engineered Nanoporous Materials. Springer.
Luechinger, N.A., Walt, S.G., Stark, W.J., 2010. Printable nanoporous silver membranes. Chem. Mater. 22, 4980–4986. https://doi.org/10.1021/cm1013152.
Luo, F., Zhang, Y., Wei, C., Zhang, C., Wang, J., Zhang, Z., 2020. On the dealloying mechanisms of a rapidly solidified Al80Ag20 alloy using in-situ X-ray diffraction. Intermetallics 125, 106913. https://doi.org/10.1016/j.intermet.2020.106913.
Maaroof, A.I., Cortie, M.B., Gentle, A., Smith, G.B., 2007. Mesoporous gold sponge as a prototype 'metamaterial'. Phys. B Condens. Matter 394, 167–170. https://doi.org/10.1016/j.physb.2006.12.014.
Maaroof, A.I., Cortie, M.B., Smith, G.B., 2005. Optical properties of mesoporous gold films. J. Opt. A: Pure Appl. Opt. 7, 303–309. https://doi.org/10.1088/1464-4258/7/7/007. https://ui.adsabs.harvard.edu/link_gateway/2005JOptA...7..303M/.
Miler, M., Mirtič, B., 2013. Accuracy and precision of EDS analysis for identification of metal-bearing minerals in polished and rough particle samples. Geologija 56, 5–17. https://doi.org/10.5474/geologija.2013.001.
Mortari, A., Maaroof, A., Martin, D., Cortie, M.B., 2007. Mesoporous gold electrodes for sensors based on electrochemical double layer capacitance. Sens. Actuators, B 123, 262–268. https://doi.org/10.1016/j.snb.2006.08.018.
Murray, J.L., 2016. Alloy Phase Diagrams. ASM Materials International, Materials Park, Ohio.

Qiu, H., Zhang, Z., Huang, X., Qu, Y., 2011. Dealloying Ag–Al alloy to prepare nanoporous silver as a substrate for surface-enhanced Raman scattering: effects of structural evolution and surface modification. ChemPhysChem 12, 2118–2123.

Ron, R., Haleva, E., Salomon, A., 2018. Nanoporous metallic networks: fabrication, optical properties, and applications. Adv. Mater. 30, 1706755 https://doi.org/10.1002/adma.201706755.

Salunkhe, R.R., Kaneti, Y.V., Yamauchi, Y., 2017. Metal–organic framework-derived nanoporous metal oxides toward supercapacitor applications: progress and prospects. ACS Nano 11, 5293–5308. https://doi.org/10.1021/acsnano.7b02796.

Sardana, N., Birr, T., Schlenker, S., Reinhardt, C., Schilling, J., 2014. Surface plasmons on ordered and bi-continuous spongy nanoporous gold. New J. Phys. 16, 063053 https://doi.org/10.1088/1367-2630/16/6/063053.

Sing, K.S., 1985. Reporting physisorption data for gas/solid systems with special reference to the determination of surface area and porosity (Recommendations 1984). Pure Appl. Chem. 57, 603–619. https://doi.org/10.1351/pac198557040603.

Song, T., Gao, Y., Zhang, Z., Zhaib, Q., 2011. Dealloying behavior of rapidly solidified Al–Ag alloys to prepare nanoporous Ag in inorganic and organic acidic media. CrystEngComm 13, 7058–7067. https://doi.org/10.1039/C1CE05538K.

Stewart, I.E., Kim, M.J., Wiley, B.J., 2017. Effect of morphology on the electrical resistivity of silver nanostructure films. ACS applied materials & interfaces 9, 1870–1876. https://doi.org/10.1021/acsami.6b12289.

Supansomboon, S., Porkovich, A., Dowd, A., Arnold, M.D., Cortie, M.B., 2014. Effect of precursor stoichiometry on the morphology of nanoporous platinum sponges. ACS Appl. Mater. Interfaces 6, 9411–9417. https://doi.org/10.1021/am501794y.

Walsh, D., Arcelli, L., Ikoma, T., Tanaka, J., Mann, S., 2003. Dextran templating for the synthesis of metallic and metal oxide sponges. Nat. Mater. 2 https://doi.org/10.1038/nmat903, 386-U5.

Wang, X., Li, R., Li, Z., Xiao, R., Chen, X.-B., Zhang, T., 2019. Design and preparation of nanoporous Ag–Cu alloys by dealloying Mg–(Ag, Cu)–Y metallic glasses for antibacterial applications. J. Mater. Chem. B 7, 4169–4176. https://doi.org/10.1039/C9TB00148D.

Wang, X., Qi, Z., Zhao, C., Wang, W., Zhang, Z., 2009. Influence of alloy composition and dealloying solution on the formation and microstructure of monolithic nanoporous silver through chemical dealloying of Al– Ag alloys. J. Phys. Chem. C 113, 13139–13150. https://doi.org/10.1021/jp902490u.

West, P.R., Ishii, S., Naik, G.V., Emani, N.K., Shalaev, V.M., Boltasseva, A., 2010. Searching for better plasmonic materials. Laser Photon. Rev. 4, 795–808. https://doi.org/10.1002/lpor.200900055.

Wittstock, A., Biener, J., Erlebacher, J., Baumer, M. (Eds.), 2012. Nanoporous Gold: from an Ancient Technology to a High-Tech Material. RSC Publishing.

Wu, T.Y., Wang, X., Huang, J.C., Tsai, W.Y., Chu, Y.Y., Chen, S.Y., DU, X.H., 2015. Characterization and functional applications of nanoporous Ag foams prepared by chemical dealloying. Metall. Mater. Trans. B 46, 2296–2304. https://doi.org/10.1007/s11663-015-0392-0.

Wu, X.-Y., Li, M.-Y., Zeng, Q.-X., Yu, Q.-X., 2022. Dense copper azide synthesized by in-situ reaction of assembled nanoporous copper microspheres and its initiation performance. Defence Technology 18, 1065–1072. https://doi.org/10.1016/j.dt.2021.05.004.

Yamauchi, I., Mase, T., Kajiwara, T., Saraoka, M., 2003. Synthesis of skeletal silver from rapidly solidified Al–Ag precursor. J. Alloys Compounds. 348, 270–277. https://doi.org/10.1016/S0925-8388(02)00798-3.

Yang, G., Fu, X.-J., Sun, J.-B., Zhou, J., 2013. Optical properties of aluminum silver alloy films deposited by magnetron sputtering. J. Alloys Compd. 547, 23–28. https://doi.org/10.1016/j.jallcom.2012.08.007.

Yang, Y., Dan, Z., Liang, Y., Wang, Y., Qin, F., Chang, H., 2019. Asynchronous evolution of nanoporous silver on dual-phase Ag–Sn alloys by potentiostatic dealloying in hydrochloric acid solution. Nanomaterials 9, 743. https://doi.org/10.3390/nano9050743.

Yuan, L., Liu, H.K., Maaroof, A., Konstantinov, K., Liu, J., Cortie, M., 2007. Mesoporous gold as anode material for lithium-ion batteries. J. of New Materials for Electrochemical Systems 10, 95–99.

Zhang, J., Li, C.M., 2012. Nanoporous metals: fabrication strategies and advanced electrochemical applications in catalysis, sensing and energy systems. Chem. Soc. Rev. 41, 7016–7031. https://doi.org/10.1039/C2CS35210A.

Zhang, Q., Zhang, Z., 2010. On the electrochemical dealloying of Al-based alloys in a NaCl aqueous solution. Phys. Chem. Chem. Phys. 12, 1453–1472. https://doi.org/10.1039/B919313H.

Zhang, R., Wang, X., Huang, J.C., Li, F., Zhang, Z., Wu, M., 2019. Formation mechanism of nanoporous silver during dealloying with ultrasonic irradiation. RSC advances 9, 9937–9945. https://doi.org/10.1039/C9RA01742A.

Zhang, Z., Ying, W., 2017. Design and fabrication of dealloying-driven nanoporous metallic electrocatalyst. Electrocatalysts for Low Temperature Fuel Cells: Fundamentals and Recent Trends 533–555. https://doi.org/10.1002/9783527803873.ch19.

Zhang, Z.H., Wang, Y., Qi, Z., Zhang, W.H., Qin, J.Y., Frenzel, J., 2009. Generalized fabrication of nanoporous metals (Au, Pd, Pt, Ag, and Cu) through chemical dealloying. J. Phys. Chem. C 113, 12629–12636. https://doi.org/10.1021/jp811445a.

Zhao, J., Tao, Z., Liang, J., Chen, J., 2008. Facile synthesis of nanoporous γ-MnO2 structures and their application in rechargeable Li-ion batteries. Cryst. Growth Des. 8, 2799–2805. https://doi.org/10.1021/cg701044b.

Zheng, L.-T., Yu-Lei, W., He-Qing, G., Lei, Q., 2013. Application progress of nanoporous gold in analytical chemistry. Chin. J. Anal. Chem. 41, 137–144. https://doi.org/10.1016/S1872-2040(13)60624-6.

Zou, X., He, Y., Sun, P., Zhao, J., Cui, G., 2018. A novel dealloying strategy for fabricating nanoporous silver as an electrocatalyst for hydrogen peroxide detection. Appl. Surf. Sci. 447, 542–547. https://doi.org/10.1016/j.apsusc.2018.04.018.

Zuruzi, A.S., Siow, K.S., 2015. Electrical conductivity of porous silver made from sintered nanoparticles. Electron. Mater. Lett. 11, 308–314. https://doi.org/10.1007/s13391-014-4357-2.